Mastering disorder in a first-order transition by ion irradiation

S. Cervera,[1] M. LoBue,[2] E. Fontana,[1,3,*] M. Eddrief,[1] V. H. Etgens,[1,†] E. Lamour,[1] S. Macé,[1] M. Marangolo,[1] E. Plouet,[1] C. Prigent,[1] S. Steydli,[1] D. Vernhet,[1] and M. Trassinelli[1,‡]

[1]*Institut des NanoSciences de Paris, CNRS, Sorbonne Université, F-75005 Paris, France*

[2]*SATIE, ENS Paris Saclay, CNRS, Université Paris-Saclay, F-91190 Gif-sur-Yvette, France*

[3]*Department of Applied Science and Technology, Politecnico di Torino, I-10129 Torino, Italy*

(Received 24 July 2023; accepted 26 January 2024; published 13 February 2024)

The effect of ion irradiation on MnAs single crystalline thin films is studied. The role of elastic collisions between ions and atoms of the material is singled out as the main process responsible for modifying the properties of the material. Thermal hysteresis suppression, and the loss of sharpness of the magnetostructural phase transition, are studied as a function of different irradiation conditions. While the latter is shown to be associated with ion-induced disorder at the scale of the transition correlation length, the former is related to the coupling between disorder and the large-scale elastic field associated with the phase coexistence pattern.

DOI: 10.1103/PhysRevMaterials.8.024406

I. INTRODUCTION

The role of quenched disorder on phase changes has been addressed theoretically for several decades [1–5]. In the case of first-order transitions, unraveling the leading physical mechanisms responsible for the coupling between random impurities and order parameters is even harder than in second-order ones. Indeed, the coexistence of different characteristic lengths and the presence of nonequilibrium features such as hysteresis and kinetics make the task even rather challenging. Nonetheless, as most of the known large caloric effects take place on the verge of a first-order ferroic transition [6], mastering hysteresis and preserving other features (i.e., entropy and temperature changes) has been the focus of many investigations for the past two decades. In addition to their fundamental interest, such investigations can have a direct impact on the use of caloric effects for refrigeration and energy conversion applications [7–9]. Hysteresis reduction in magnetocaloric materials has been successfully achieved by acting on the phase transition globally, getting closer to a critical point through chemical change [10,11], using a secondary external field [12–14], or using local nonhomogeneity fostering phase nucleation. Indeed, controlling first-order phase changes in caloric materials using defects and disorder has been studied at different scales, from the atomic/chemical scale [15,16] to the structural one [17,18]. Therefore, the possibility of tuning the amount of disorder in a model system represents a unique opportunity for experimental investigations on phase change in solid-state systems. Moreover, it can pave the way for developing new methods for tailoring the functional properties of materials where phase changes take place.

In this paper, we study the modifications induced by the collision and implantation of ions in manganese arsenide thin monocrystals. Bulk manganese arsenide (MnAs) shows a first-order magnetostructural transition from ferromagnetic to paramagnetic order accompanied by a lattice symmetry switch when getting above the transition temperature $T_t = 313$ K [19]. From this perspective, MnAs can be considered as a prototypical first-order magnetocaloric material. Previous studies [20,21] proved thermal hysteresis suppression in ion-irradiation MnAs films, keeping the caloric effect intensity unchanged. Here the mechanisms underlying the modifications of the transition after ion irradiation are investigated on single crystalline 150-nm-thick MnAs films under different irradiation conditions (i.e., ion mass, ion kinetic energy, fluences, etc.).

II. EXPERIMENTAL METHODS

A. Growth conditions

The MnAs films have been produced by molecular beam epitaxy on GaAs(001) 0.3-mm-thick substrates with the α-MnAs[0001] axis parallel to GaAs[$\bar{1}$10] [22]. Due to the epitaxial strain, the phase coexistence between the ferromagnetic α-phase with hexagonal structure (NiAs-type) and the paramagnetic β-phase with orthorhombic structure, (MnP-type) takes place over an extended temperature range (280–320 K) [23], in contrast with the sharper transition observed at the temperature $T_t = 313$ K in bulk single crystals [24]. This widening of the phase-coexistence region is characterized by a linear evolution of the phase fraction, across the transition, as a function of T. As shown in [25–29], this behavior is driven by a mesoscopic phase coexistence pattern often referred to as stripes-domain pattern [22], and by its long-range elastic field.

B. Irradiation conditions

Ion irradiation has been performed at two facilities: the electron-cyclotron ion source SIMPA facility (Paris, France) [30], and the line IRRSUD facility at the GANIL accelerator (Caen, France).

*Present address: Institut Néel, CNRS, F-38042 Grenoble, France.

†Present address: Centre de Recherche et de Restauration des Musées de France, F-75001 Paris, France.

‡martino.trassinelli@insp.jussieu.fr

TABLE I. Summary of the irradiation characteristics ordered by the density of the induced collisions. Fluence and flux values indicate the corresponding average value during the irradiation.

Coll. density (cm^{-3})	Ion density (cm^{-3})	Ion	At. mass	Kin. energy (keV)	Incident angle (deg)	Fluence (ions cm^{-2})	Flux (ions $cm^{-2}\,s^{-1}$)
4.83×10^{19}	0.00	Ar	36	7800	0	4.00×10^{12}	6.67×10^{9}
6.60×10^{19}	1.97×10^{16}	Ar	40	208	60	3.64×10^{11}	2.43×10^{10}
1.85×10^{20}	1.49×10^{18}	He	4	22	60	3.27×10^{13}	6.54×10^{12}
2.41×10^{20}	0.00	Ar	36	7800	0	2.00×10^{13}	6.06×10^{9}
4.71×10^{20}	9.17×10^{16}	Kr	84	260	0	1.40×10^{12}	9.33×10^{10}
7.18×10^{20}	6.70×10^{17}	O	16	84	60	1.34×10^{13}	1.12×10^{12}
9.37×10^{20}	6.54×10^{17}	Ne	20	89	60	1.32×10^{13}	1.96×10^{11}
1.07×10^{21}	7.44×10^{17}	Ne	20	90	60	1.50×10^{13}	2.50×10^{11}
1.21×10^{21}	0.00	Ar	36	7800	0	1.00×10^{14}	4.57×10^{9}
2.69×10^{21}	5.24×10^{17}	Kr	84	260	0	8.00×10^{12}	8.00×10^{10}
3.47×10^{21}	1.04×10^{18}	Ar	40	208	60	1.91×10^{13}	3.19×10^{11}
6.31×10^{21}	1.89×10^{18}	Ar	40	208	60	3.48×10^{13}	2.32×10^{10}
7.66×10^{21}	5.34×10^{18}	Ne	20	89	60	1.08×10^{14}	1.80×10^{11}
3.26×10^{22}	2.63×10^{20}	He	4	22	60	5.76×10^{15}	6.40×10^{12}
4.82×10^{22}	9.36×10^{18}	Kr	84	260	0	1.43×10^{14}	1.19×10^{11}
1.56×10^{23}	4.65×10^{19}	Ar	40	208	60	8.59×10^{14}	5.72×10^{10}

At SIMPA, samples have been irradiated with different ions (helium, oxygen, neon, argon, and krypton) with kinetic energies ranging from 22 to 260 keV. The ion fluence Φ has been varied between 1×10^{12} and 6×10^{15} ions/cm^2, corresponding to an irradiation time spanning from few tens of seconds up to several hours. All irradiation have been performed at room temperature. The energy of the different ion beams and the incident angle have been chosen in order to reach an average penetration depth corresponding to the half thickness of the film.

At IRRSUD a beam of isotopic ^{36}Ar with an energy of 35.28 MeV has been used. In this case, no ions are implanted in the MnAs film, with most of them being stopped in the GaAs substrate. The fluence has been varied from 4×10^{12} to 5×10^{15} ions/cm^2. The complete information about the irradiation conditions can be found in Table I.

During the interaction with a solid, the ion transfers its kinetic and potential energies to the target atoms by a series of processes that can be schematically separated into two categories: one due to the interaction with the target nuclei, and the other due to the interaction with the electrons. The electron interaction is inelastic, and it entails small or no lattice distortion into the target. The ion energy losses, including those related to the potential energy of the ion, are transferred to the solid via excitation of phonons, with an increase in temperature along the trajectory. Nuclear collisions are the most probable process at low velocity and/or for heavy ions [31–33]. Such collisions lead to the displacement of sample atoms from their site, and, if the kinetic energy is sufficiently high, to a cascade of secondary collisions, with the creation of clusters of vacancies and interstitial atoms in the sample lattice [31]. For the same kinetic energy, heavy ions produce a higher number of collisions per ion than light ions. This is due to the higher cross-section of the primary impact and the more favorable momentum transfer to target atoms, as well as the consequent secondary collisions in the cascade.

At the ion kinetic energies of SIMPA ($E_{\rm kin}$ less than 300 keV), the main process responsible for induced modifications is the nucleus-nucleus interaction between incoming ions and sample atoms. At the ion kinetic energies of IRRSUD, the probability of nuclear processes decreases while inelastic processes start to occur. Due to the small ion potential energy ($E_p \lesssim 5$ keV), compared to the kinetic energy, and to the metallic nature of the MnAs samples, the local heating from the electron interaction is not expected to induce noticeable modifications in the material. Indeed, elastic nuclear collisions remain the leading process that modifies the properties of the irradiated sample.

III. RESULTS AND DISCUSSIONS

A. General considerations

The two main modifications observed after ion irradiation are hysteresis reduction and the loss of sharpness of the transition, often referred to as *rounding* [2] (see Fig. 1). To investigate them, isofield thermomagnetic $M(T)$ curves have been measured at constant field $H = 1$ T by a SQUID device with H parallel to the in-plane easy magnetization direction. This makes the proportionality between $M(T)$ and the ferromagnetic α-phase a reliable assumption even under the application of a relatively small field of 1 T. Before each measurement, the material has been heated up to 350 K in order to erase any trace of the low-temperature phase, resetting the sample history [34]. Hysteresis, transition temperatures, and rounding are extracted from the $M(T)$ curves and from their derivatives. Whereas hysteresis, and its reduction, are phenomena taking place close to the transition temperature T_t, the transition rounding is associated with a widening of the phase-coexistence region far away from it. Here, the thermal hysteresis width, $\Delta T_{\rm hyst}$, is evaluated from the area A between the $M(T)$ heating and cooling curves (Fig. 1, top) normalized to the saturation magnetization M_s measured at 100 K with $\Delta T_{\rm hyst} = A/M_s$. This is an approach commonly used in the field of loss and hysteresis modeling; it amounts to considering the effective width of an equivalent

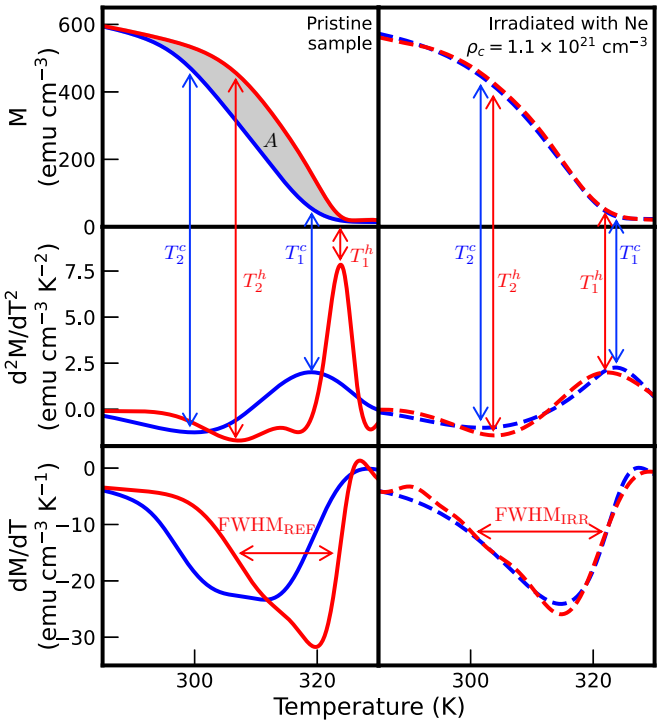

FIG. 1. Magnetization curves $M(T)$ (top) and corresponding first (bottom) and second derivative (middle) measured on reference (left) and irradiated (right) samples. Examples of FWHM$_{REF}$ and of FWHM$_{IRR}$, used in Eq. (1), are depicted in the bottom frame, left and right, respectively. The temperatures T_1^h and T_1^c corresponding to the maximum of the second derivative d^2M/dT^2 under heating and cooling, respectively, are chosen to represent the upper limit of the phase-coexistence interval. Similarly, T_2^h and T_2^c, corresponding to the minima of the second derivative under heating and cooling, respectively, mark the lower bound of the same interval. The area A of the thermal hysteresis loop has been shaded in the upper frame. Cooling and heating curves are represented in blue and red, respectively.

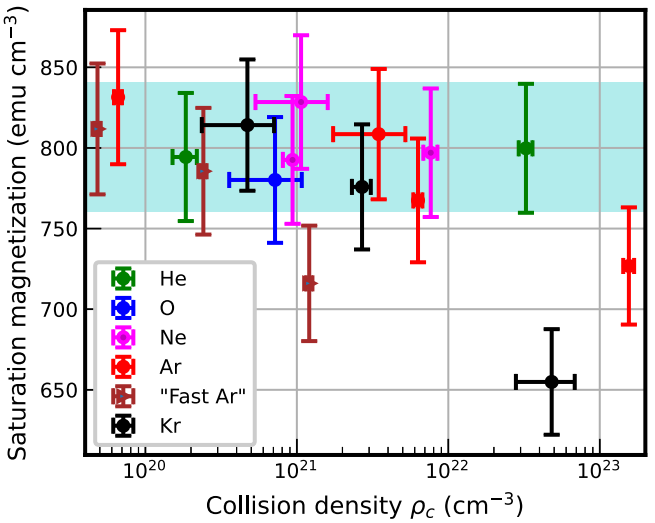

FIG. 2. Saturation magnetization (measured with $H = 1$ T at 100 K) as a function of the collision density.

rectangular hysteresis cycle [35,36]. Indeed, most samples have been irradiated within regimes where the maximum magnetization M_s is not, or is marginally, modified, as is visible in Fig. 2. From the almost unchanged value of M_s and from previous x-ray diffraction characterizations of the film structure after irradiation with neon ions up to a fluence equal to 1.5×10^{15} ions/cm^2 [20], no amorphization of the samples is expected.

Concerning the evaluation of the rounding, the data analysis has to disentangle the effect due to defects-induced disorder [13,37] from the strain-induced broadening at the magnetostructural phase transition. The latter is driven by the above-mentioned mesoscopic phase-coexistence domain pattern. The former is relevant far from T_t and is associated with the presence of minority-phase regions whose stability is made possible by a local shift of T_t [2]. To tag the irradiation rounding effect only, we introduce the variable

$$\Delta T_{\rm rnd} = \mathrm{FWHM_{IRR}} - \mathrm{FWHM_{REF}} \qquad (1)$$

obtained by the full width at half-maximum (FWHM$_{IRR}$) of the first derivative of $M(T)$ of the irradiated films minus the contribution FWHM$_{REF}$ of the pristine sample (see Fig. 1, bottom). The second derivative d^2M/dT^2 is used to identify the main part of the phase coexistence interval bounded by the maximum (at the temperature T_1) and the minimum (at T_2) of d^2M/dT^2, respectively. Some typical irradiation-induced modifications are presented as an example in Fig. 1, where the extrema of d^2M/dT^2 under heating (T_1^h, and T_2^h) and cooling (T_1^c, and T_2^c) are marked over the $M(T)$ of the pristine and of an irradiated sample.

B. Hysteresis: Implanted ions vs induced collisions

To disentangle the role of binary-collisions-induced defects from that of ion implantation in modifying the target properties, we first compare sample features with respect to the average collision density or to the implanted ion density, ρ_c and ρ_i, respectively. These quantities are estimated using the applied ion fluences, and the output of the ion-matter interaction Monte Carlo code SRIM/TRIM [38,39]. More precisely, the outputs from the *Detailed Calculation with Full Damage Cascades* mode are considered, which include the position and number of the produced defects. ρ_c is obtained from vacancies and interstitial defects. The two densities induced by irradiating a sample of thickness t with a fluence Φ are estimated through the following expressions: $\rho_i = f\Phi/t$ and $\rho_c = N_{\rm coll}\Phi/t$, where f is the fraction of ions stopped, and $N_{\rm coll}$ is the average number of binary collisions induced by a single ion in the film. Note that with this simple approach, we do not take into account the depth dependencies of the implanted ion and induced collision densities, but only their average values. For irradiations with slow ions, such inhomogeneities can be very important but are not considered in our analysis. Such an effect is normally attenuated by the possible migration of defects, which is not considered as well. More specifically, for MnAs thin films, characterized by regular volumetric self-organization of the different phases, irradiation-induced defects at a specific depth are expected to affect the whole sample thickness.

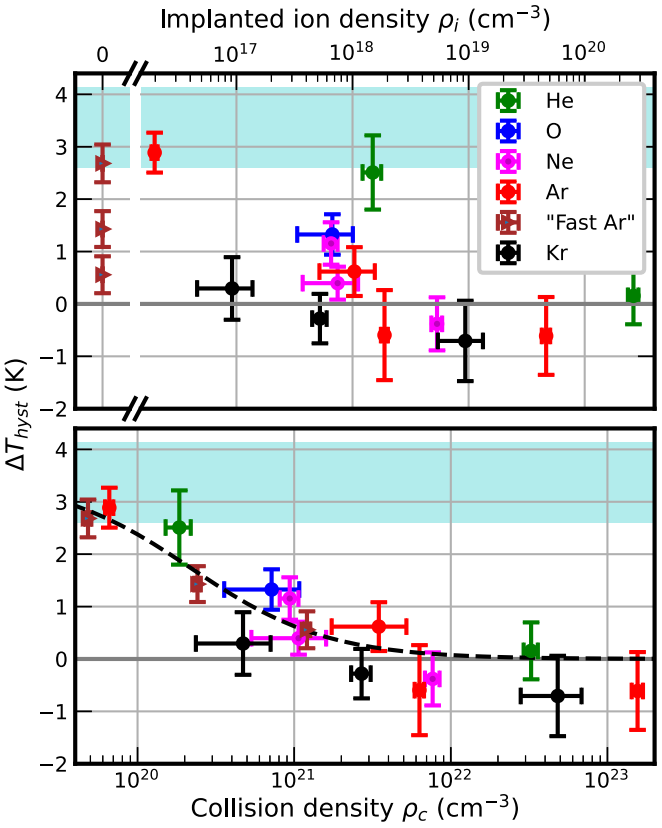

FIG. 3. Thermal hysteresis area as a function of the average density of implanted ions ρ_i (top), and of the average density of elastic collisions ρ_c (bottom). In light blue, the value of the pristine sample is reported. The uncertainties on the x-axis are mainly determined by the fluence evaluation, which can be critical for some beam preparation. The uncertainty on the y-axis is due to the SQUID measurement and the interpolation of the data affected by noise. The dashed line represents the best fit of the data with the formula discussed in the text.

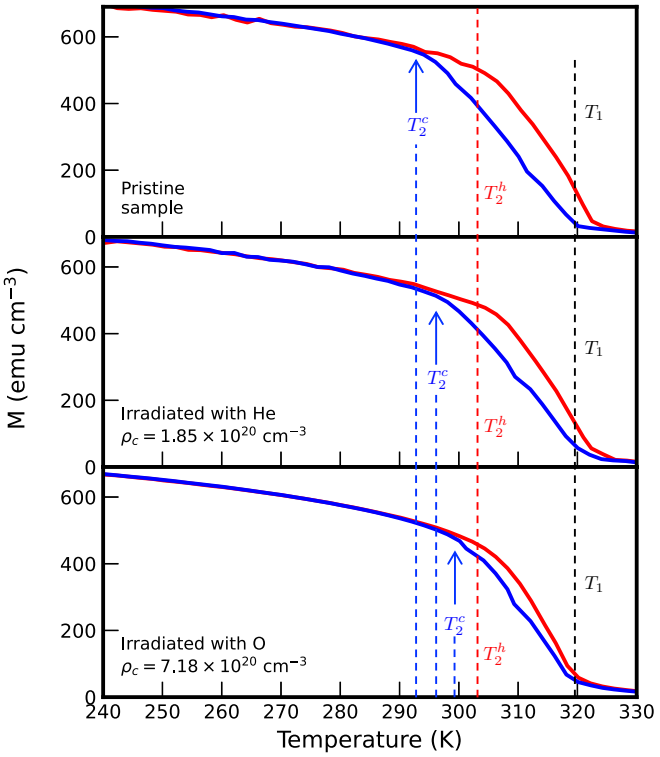

FIG. 4. Comparison between $M(T)$ loops over heating and cooling (in red and blue), measured on the pristine sample (top), on a He irradiated sample (middle), and on an O irradiated sample (bottom). As is apparent from Fig. 5, ΔT_1 is rather small and does not show any clear trend as a function of the collision density. Thence, a single dashed black line is used to mark T_1 over all the curves. On the contrary, ΔT_2 reduces as a function of ρ_c. Furthermore, this reduction takes place at fixed T_2^h (i.e., the single dashed red line), with T_2^c getting higher and closer to T_2^h as a function of the collision density (i.e., as shown by the sequence of blue dashed lines in the three frames of the figure).

Despite the well-known SRIM/TRIM trend of slightly overestimating the number of induced defects [31,33,40], the predicted agglomerations (i.e., mixed-up vacancies and interstitials clusters) are rather similar to the ones obtained by advanced many-body molecular-dynamics calculations, taking into account collective behavior and temperature effects [32,33,41–43], and to the ones observed experimentally as well [44]. For our specific cases, f and N_{coll} have a range of [0, 1] and [50,5000], respectively. Thus, ρ_i and ρ_c differ by orders of magnitude and depend strongly on the projectile ion characteristics.

In Fig. 3 we can see that, whereas no correlation is apparent between ΔT_{hyst} and ρ_i, a clear trend can be appreciated when ΔT_{hyst} is plotted against ρ_c. More precisely, ΔT_{hyst} decreases as a function of ρ_c until its total suppression at $\rho_c \approx 10^{21}$–10^{22} cm^{-3}. It is noteworthy that the three points relative to fast Ar irradiation, where no ions get implanted into the sample, spread over the same hysteresis decreasing trend curve when plotted against ρ_c. This is one of the main findings of this study, and it shows that the relevant defects are the ones produced by binary elastic collisions.

C. Hysteresis: Additional insights

To get a better insight into the mechanisms underlying thermal hysteresis in MnAs films, the amplitude of the phase coexistence interval is studied over heating and cooling as a function of ρ_c. When hysteresis is present, the aforementioned second derivative maximum and minimum show different values along the cooling and heating curves (see Fig. 4; additional curves can be found in [45]).

More precisely, the upper limit of the phase coexistence interval under heating, T_1^h, and cooling T_1^c are rather similar, and their difference $\Delta T_1 = T_1^h - T_1^c$, shown in Fig. 5 (bottom), stays close to zero in all samples, and does not show any specific trend as a function of the collision density ρ_c. On the contrary, the difference $\Delta T_2 = T_2^h - T_2^c$ between T_2 over heating, and cooling shown in Fig. 5 (top) is relevant in the pristine sample and gets reduced, and eventually suppressed, as a function of ρ_c following a trend similar to the one of ΔT_{hyst}. In Fig. 4, the values of T_2^h and T_2^c are marked with dashed lines (red and blue, respectively) over the $M(T)$ curves of different samples. In the same figure, a single black dashed line marks T_1 over the reference and the irradiated samples. Following [26], T_1 can be considered the closest approximation to the

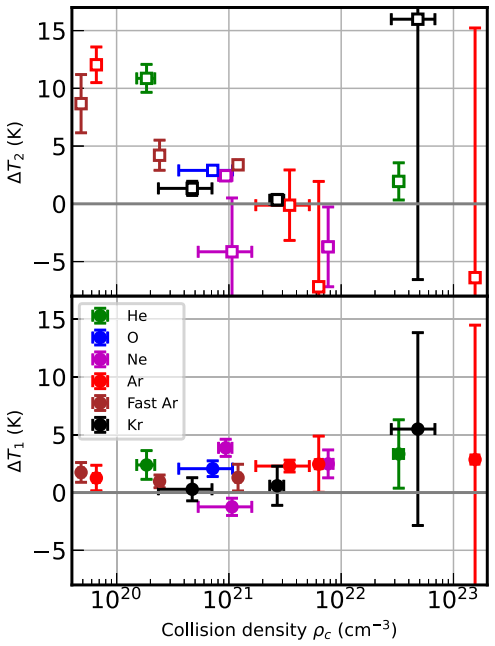

FIG. 5. Differences $\Delta T_2 = T_2^h - T_2^c$ (top) and $\Delta T_1 = T_1^h - T_1^c$ (bottom) between the extrema of the coexistence interval over heating and cooling as a function of ρ_c. $\Delta T_2 = T_2^h - T_2^c$ reduces as a function of ρ_c, similarly to ΔT_{hyst}. ΔT_1 instead is, on average, close to 0, and does not show any specific trend as a function of ρ_c.

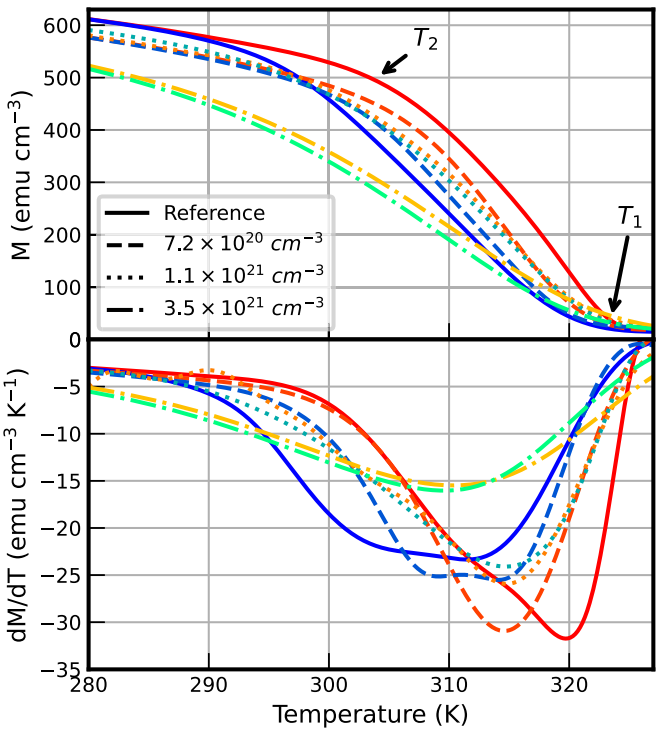

FIG. 6. Isofield ($H = 1$ T) magnetization curves $M(T)$ (top) and their first derivative (bottom) measured on reference (continuous lines) and irradiated (dashed lines) samples. Warm and cold colors correspond to heating and cooling curves, respectively.

actual transition point T_t (i.e., the one of a bulk single crystal). On the other hand, as is apparent from Fig. 4, the reduction of hysteresis takes place as an increase of T_2^c in irradiated samples, with no change of T_2^h. In other words, hysteresis disappears through the collapse of the cooling $M(T)$ curve onto the heating one. Hence, hysteresis is mainly associated with supercooled metastable states.

Hysteresis is suppressed by ion-irradiation within the collision density interval 3×10^{20} cm$^{-3} \lesssim \rho_c \lesssim 10^{21}$ cm^{-3} (see Fig. 3). However, as was clearly put in [26], thermal hysteresis takes place in a temperature interval where the material behavior is driven by the self-organized phase-coexistence pattern, a state of affairs that can hardly be explained through a droplet-nucleation mechanism.

While only the cooling dM/dT curve plotted in Fig. 1 (bottom) for the nonirradiated sample shows a good agreement with the linear phase-evolution picture described in Refs. [25,26], all the other curves show a nonlinear $M(T)$. In addition, Figs. 1 (bottom) and 6 show that the hysteresis reduces jointly with the loss of linearity of the cooling $M(T)$ curve with higher values of the maximum of dM/dT, implying sharper phase kinetics as a function of T. Similar asymmetries are a rather common feature of first-order phase transitions, from the best-known example of the water-ice transition to the different kinetics observed under cooling, and heating in FeRh films [46]. Here, as is noticeable in Fig. 4, the difference between the cooling and heating $M(T)$ curves depends on the lower slope of the former, and on the entailed lower T_2 (i.e., a coexistence region lasting till a lower temperature). The loss of linearity and the increasing slope, going hand-in-hand with the hysteresis reduction, take place where the kinetics is led by the stripes domain elastic field. Therefore, all these modifications can be interpreted as a modification of the elastic field associated with the stripes.

A possible clue to explain this behavior comes from the observation of the distortion of the regular stripes pattern in MnAs films after ion irradiation [20], with an increasing density of finite-length stripes. These defects have been observed in nonirradiated samples too [22,28,29]. They are associated with the nonlinear region of $M(T)$ and they mostly disappear within the ordered-stripes structure getting closer to the transition temperature. Finite-length stripes may behave as topological defects, modifying the elastic energy with their stress field, similarly to the way unbound edge-dislocations do in 3D solids [47,48], and in 2D mesomorphic phases [49]. Their increased density in irradiated samples can be the origin of the suppression of the supercooled metastable states, either by changing the phase fraction through nucleation of pairs or by renormalizing the effective elastic constants.

This explanation, in spite of its being still rather conjectural, raises the question of the way ion-induced disorder directly modifies the phase-domain patterning where the relevant scale is the phase-domain characteristic length (i.e., the stripes spacing, $d_s \approx 0.73\,\mu$m [20]).

It is worth noting that, as shown in [25,26], the stripe phase-domains in MnAs show a regular spacing driven by the substrate elastic field, and fully determined by the film thickness. From this standpoint, the appearance of an increasing number of topological defects within the pattern after ion irradiation, as reported in [20], is the signature of a global modification of the pattern involving the full thickness of the

film. Putting it another way, hysteresis reduction is associated with a change in the stripes pattern behaving as a 2D mesostructure, notwithstanding the depth distribution of the collision-induced impurities.

Over such a large scale, the average collision density $\rho_c \propto p$, with p the probability to get a lattice site occupied by some sort of impurity, is expected to be the relevant quantity determining the topological defects density. Nonetheless, some preexisting defect density, associated with an intrinsic impurity density p_0 present in the reference sample, must be considered. The dashed curve in Fig. 3 (bottom), describing the hysteresis reduction as a function of the collision density ρ_c, is obtained using the following fitting function:

$$f(\rho_c) \propto \frac{1}{p_0 + p} = \frac{1}{p_0 + a\,\rho_c/\rho_0}, \tag{2}$$

where $\rho_0 = 2.92\times10^{22}$ cm^{-3} is the atomic density of MnAs, a is a proportionality constant between p and ρ_c/ρ_0 that incorporates possible autohealing processes, not taken into account by SRIM/TRIM, and possible activation thresholds, and p_0 is a constant describing the impurities present in the sample before the irradiation. When the value $a = 9.7\%$, determined from the rounding analysis (see the next section), is used, the probability value $p_0 = (7.3 \pm 2.3)\times10^{-4}$ for the impurity density in the pristine sample is found. This relatively low value is consistent with the typical values of molecular beam epitaxial samples [50], and with its nearly defect-free stripe pattern reported in [20]. It shows that, besides reducing hysteresis, collision-induced defects can be used to tailor the film domain pattern in the phase-coexistence region.

Considering ρ_c as a figure of merit is equivalent to considering the total volume $\langle V_{\rm cas}\rangle$ of the ion-induced collisional cascades like in the Gibbons model [31,51]. The collision density is, in fact, proportional to $N_{\rm coll}\phi/t$, where t is the thickness of the sample, ϕ is the ion fluence, and $N_{\rm coll}$ is the number of collisions per ion, expected to be proportional to the single ion cascade $\langle V_{\rm cas}\rangle$. Due to the relatively small value of ρ_c corresponding to the hysteresis disappearing, effects due to cascade overlaps can be excluded.

D. Rounding

The transition rounding $\Delta T_{\rm rnd}$, deduced from Eq. (1), also shows a systematic trend as a function of the collision density ρ_c (Fig. 7, top). Its departure from the reference value, at $\rho_c \approx 4\times10^{20}$ cm^{-3}, is followed by a strong increase with a slope depending on the ion type used for irradiation. Furthermore, the points collapse over the same curve when normalizing the relative rounding to the square root of the ion mass number m, $\Delta T_{\rm rnd}/\sqrt{m}$ (Fig. 7, bottom).

Differently from hysteresis suppression, which takes place near T_t where stripe domains and their long-range elastic field drive transition kinetics at the mesoscale [26], rounding takes place far from T_t where the only relevant scale is the phase-transition correlation length ξ. Indeed, the rounding behavior fits quite well within the approach reported in [2].

Considering a magnetic lattice model with a probability p to get a lattice site occupied by some sort of impurity, it is shown that, even when $p \ll 1$, a relevant transition rounding can appear due to the local fluctuations of impurity

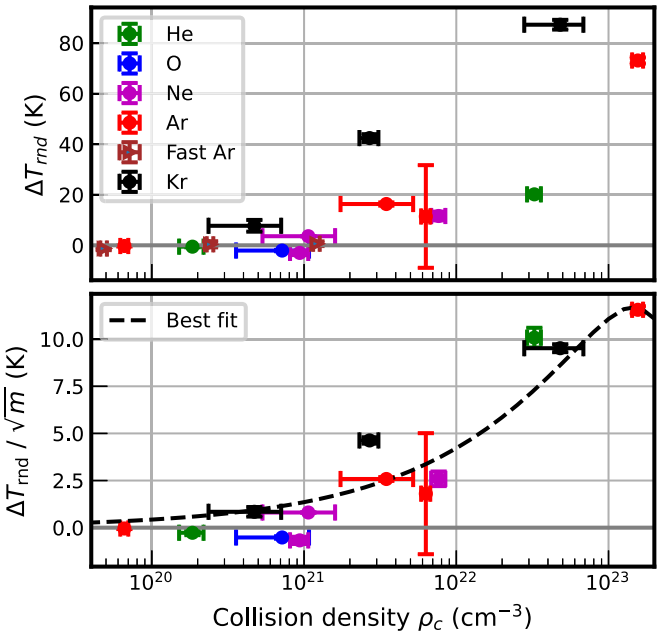

FIG. 7. Relative rounding $\Delta T_{\rm rnd}$ from the FWHM of dM/dT curves without (top) and with $\sqrt{m}$) mass rescaling (bottom). The dashed line represents the best fit of the data with the function $f(p) = c\sqrt{p(1-p)}$ (see text).

density. For a random impurity distribution, density fluctuations are proportional to the variance $p(1-p)$. The key issue to get a stable rounding is the relationship between the phase-transition correlation length ξ and the characteristic size L of the regions where the impurity density fluctuation makes the minority phase energetically favored. Therefore, the smearing-out of the transition is driven by the dimensionality d of the magnetic system, and by the way the interface energy between the two phases scales with respect to the region size L. Following [2], a spin lattice of dimensionality $d = 3$, with discrete symmetry, and with a surface tension between phases over a region of size L scaling as L^2, is expected to be unaffected by quenched disorder when $L < \xi$. Rounding appears when $L \sim \xi$, and it scales as $\sqrt{p(1-p)/L^3}$ when $L > \xi$. Assuming the probability p, to get an impurity to be $p \propto \rho_c$, from Fig. 7 it can be deduced that $\xi \sim L$ when $\rho_c \approx 4\times10^{20}$ cm^{-3}. From cascade simulations, one can observe that one single ion forms several clusters of defects. The typical volume of collision clusters is $\propto 1/m$, where m is the ion mass. Assuming elastic-collision cascades as the origin of the impurities implies $L^3 \propto 1/m$, a feature that explains the higher slopes shown by samples irradiated with heavier ions and the collapse of all the points onto the same curve after the $1/\sqrt{m}$ normalization. Similar curves can be obtained by normalizing with respect to the number of collisions per ion and the average size of clusters of defects. Figure 7 (bottom) shows the mass normalized relative rounding data fitted with a function

$$f(\rho_c) = c\sqrt{a\frac{\rho_c}{\rho_0}\left(1 - a\frac{\rho_c}{\rho_0}\right)} \equiv c\sqrt{p(1-p)}. \tag{3}$$

From this analysis, a value of $a = (9.7 \pm 0.6)\%$ is found.

This shows that far away from the transition temperature, the minority phase develops as randomly distributed droplets before the building-up of the elastic-domain stripe structure as reported in [27,29]. Whereas closer to T_t energy minimization is dominated by the long-range elastic interaction between stripes [25], in the first stages of the transition the leading energy terms are local, and fully led by the size L of regions where the precursor develops.

For the high-fluence regime considered for the rounding effect, one could also consider the effect of the collisional cascade overlapping. When we consider the simple model from Gibbons [31,51], the fraction of the irradiated volume V_I over the total sample volume V_0 is given by

$$\frac{V_I}{V_0} = 1 - e^{-\frac{\langle V_{\rm cas}\rangle \phi}{t}} = 1 - e^{-C\rho_c}, \tag{4}$$

with $\langle V_{\rm cas}\rangle$ the average cascade volume, ϕ the ion fluence, and t the sample thickness. Introducing an appropriated constant C, this formula can be written in terms of collision density ρ_c (see the previous section) and thus it should be independent of the ion type. However, this approach does not consider the cascade fragmentation into defect clusters that is taken into account in our analysis by the $\sqrt{m}$ dependence. Except for the very high density values of ρ_c, most of the data described here are expected to be in the regime with $p = a\rho_c/\rho_0 \ll 1$, where cascade overlapping can be neglected.

IV. CONCLUSIONS

In this work, we address the changes induced in MnAs thin films by ion irradiation. It is shown that elastic ion-atom collisions are the main mechanism responsible for modifying the magnetic properties of the material. In addition, modifications induced by ion collisions are shown to act at two different scales. In the short range, collisions serve as nucleation seeds of precursors responsible for the loss of sharpness of the phase change far from the transition temperature. At a larger scale, collisions modify the elastic energy by softening the long-range elastic field associated with the substrate coupling. Thus, the creation of new topological defects is favored in a distorted stripe pattern, and the thermal hysteresis is reduced until its elimination.

Disorder induced by light ion irradiation of magnetic thin films has been recently investigated through domain-wall motion measurements focusing on spintronics applications [52]. Here, the effect of irradiation with ions of different mass is investigated through the behavior of the first-order magnetostructural transition on MnAs thin epitaxial films. Hysteresis suppression, transition rounding, and the tailoring of the phase-domain pattern are observed, opening unique opportunities in terms of applications to magnetocaloric devices, and to the design of novel magnetic heterostructures.

ACKNOWLEDGMENTS

The authors acknowledge the staff (and in particular D. Hrabovsky) of the MPBT (physical properties–low temperature) platform of Sorbonne Université for their support. This work was supported by French state funds managed by the ANR within the Investissements d'Avenir programme under Reference No. ANR-11-IDEX-0004-02, and within the framework of the Cluster of Excellence MATISSE (10-LABX-0067) led by Sorbonne Universités, and of the project HiPerTher-Mag (ANR-18-CE05-0019).

[1] A. B. Harris, Effect of random defects on the critical behaviour of Ising models, J. Phys. C **7**, 1671 (1974).

[2] Y. Imry and M. Wortis, Influence of quenched impurities on first-order phase transitions, Phys. Rev. B **19**, 3580 (1979).

[3] J. P. Sethna, K. Dahmen, S. Kartha, J. A. Krumhansl, B. W. Roberts, and J. D. Shore, Hysteresis and hierarchies: Dynamics of disorder-driven first-order phase transformations, Phys. Rev. Lett. **70**, 3347 (1993).

[4] A. Berger, A. Inomata, J. S. Jiang, J. E. Pearson, and S. D. Bader, Experimental observation of disorder-driven hysteresis-loop criticality, Phys. Rev. Lett. **85**, 4176 (2000).

[5] T. R. Kirkpatrick and D. Belitz, Stable phase separation and heterogeneity away from the coexistence curve, Phys. Rev. B **93**, 144203 (2016).

[6] X. Moya, S. Kar-Narayan, and N. D. Mathur, Caloric materials near ferroic phase transitions, Nat. Mater. **13**, 439 (2014).

[7] O. Gutfleisch, T. Gottschall, M. Fries, D. Benke, I. Radulov, K. P. Skokov, H. Wende, M. Gruner, M. Acet, P. Entel, and M. Farle, Mastering hysteresis in magnetocaloric materials, Philos. Trans. R. Soc. A **374**, 20150308 (2016).

[8] J. Lyubina, Magnetocaloric materials for energy efficient cooling, J. Phys. D **50**, 053002 (2017).

[9] T. Gottschall, K. P. Skokov, M. Fries, A. Taubel, I. Radulov, F. Scheibel, D. Benke, S. Riegg, and O. Gutfleisch, Making a cool choice: The materials library of magnetic refrigeration, Adv. Energy Mater. **9**, 1901322 (2019).

[10] E. Brück, N. T. Trung, Z. Q. Ou, and K. H. J. Buschow, Enhanced magnetocaloric effects and tunable thermal hysteresis in transition metal pnictides, Scr. Mater. **67**, 590 (2012).

[11] V. Franco, J. S. Blázquez, J. J. Ipus, J. Y. Law, L. M. Moreno-Ramírez, and A. Conde, Magnetocaloric effect: From materials research to refrigeration devices, Prog. Mater. Sci. **93**, 112 (2018).

[12] J. Liu, T. Gottschall, K. P. Skokov, J. D. Moore, and O. Gutfleisch, Giant magnetocaloric effect driven by structural transitions, Nat. Mater. **11**, 620 (2012).

[13] D. H. Mosca, F. Vidal, and V. H. Etgens, Strain engineering of the magnetocaloric effect in MnAs epilayers, Phys. Rev. Lett. **101**, 125503 (2008).

[14] X. Moya, L. E. Hueso, F. Maccherozzi, A. I. Tovstolytkin, D. I. Podyalovskii, C. Ducati, L. C. Phillips, M. Ghidini, O. Hovorka, A. Berger, M. E. Vickers, E. Defay, S. S. Dhesi, and N. D. Mathur, Giant and reversible extrinsic magnetocaloric effects in $La_{0.7}Ca_{0.3}MnO_3$ films due to strain, Nat. Mater. **12**, 52 (2013).

[15] V. V. Sokolovskiy, V. D. Buchelnikov, M. A. Zagrebin, P. Entel, S. Sahoo, and M. Ogura, First-principles investigation of chemical and structural disorder in magnetic $Ni_2Mn_{1+x}Sn_{1-x}$ heusler alloys, Phys. Rev. B **86**, 134418 (2012).

[16] A. Fujita, D. Matsunami, and H. Yako, Realization of small intrinsic hysteresis with large magnetic entropy change in $La_{0.8}Pr_{0.2}(Fe_{0.88}Si_{0.10}Al_{0.02})_{13}$ by controlling itinerant-electron characteristics, Appl. Phys. Lett. **104**, 122410 (2014).

[17] J. Lyubina, Recent advances in the microstructure design of materials for near room temperature magnetic cooling, J. Appl. Phys. **109**, 07A902 (2011).

[18] R. Niemann, S. Hahn, A. Diestel, A. Backen, L. Schultz, K. Nielsch, M. F.-X. Wagner, and S. Fähler, Reducing the nucleation barrier in magnetocaloric heusler alloys by nanoindentation, APL Mater. **4**, 064101 (2016).

[19] N. Menyuk, J. A. Kafalas, K. Dwight, and J. B. Goodenough, Effects of pressure on the magnetic properties of MnAs, Phys. Rev. **177**, 942 (1969).

[20] M. Trassinelli, M. Marangolo, M. Eddrief, V. H. Etgens, V. Gafton, S. Hidki, E. Lacaze, E. Lamour, C. Prigent, J.-P. Rozet, S. Steydli, Y. Zheng, and D. Vernhet, Suppression of the thermal hysteresis in magnetocaloric MnAs thin film by highly charged ion bombardment, Appl. Phys. Lett. **104**, 081906 (2014).

[21] M. Trassinelli, L. B. Carlsson, S. Cervera, M. Eddrief, V. H. Etgens, E. V. Gafton, E. Lacaze, E. Lamour, A. Lévy, S. Macé, C. Prigent, J. P. Rozet, S. Steydli, M. Marangolo, and D. Vernhet, Low energy ne ion beam induced-modifications of magnetic properties in MnAs thin films, J. Phys.: Condens. Matter **29**, 055001 (2017).

[22] R. Breitwieser, F. Vidal, I. L. Graff, M. Marangolo, M. Eddrief, J-.C. Boulliard, and V. H. Etgens, Phase transition and surface morphology of MnAs/GaAs (001) studied with in situ variable-temperature scanning tunneling microscopy, Phys. Rev. B **80**, 045403 (2009).

[23] L. Däweritz, Interplay of stress and magnetic properties in epitaxial MnAs films, Rep. Prog. Phys. **69**, 2581 (2006).

[24] R. H. Wilson and J. S. Kasper, The crystal structure of mnas above 40 °C, Acta Cryst. **17**, 95 (1964).

[25] V. M. Kaganer, B. Jenichen, F. Schippan, W. Braun, L. Däweritz, and K. H. Ploog, Strain-mediated phase coexistence in heteroepitaxial films, Phys. Rev. Lett. **85**, 341 (2000).

[26] V. M. Kaganer, B. Jenichen, F. Schippan, W. Braun, L. Däweritz, and K. H. Ploog, Strain-mediated phase coexistence in MnAs heteroepitaxial films on GaAs: An x-ray diffraction study, Phys. Rev. B **66**, 045305 (2002).

[27] T. Plake, M. Ramsteiner, V. M. Kaganer, B. Jenichen, M. Kästner, L. Däweritz, and K. H. Ploog, Periodic elastic domains of coexisting phases in epitaxial MnAs films on GaAs, Appl. Phys. Lett. **80**, 2523 (2002).

[28] T. Plake, T. Hesjedal, J. Mohanty, M. Kästner, L. Däweritz, and K. H. Ploog, Temperature-dependent magnetic force microscopy investigation of epitaxial MnAs films on GaAs (001), Appl. Phys. Lett. **82**, 2308 (2003).

[29] L. Däweritz, M. Kästner, T. Hesjedal, T. Plake, B. Jenichen, and K. H. Ploog, Structural and magnetic order in MnAs films grown by molecular beam epitaxy on GaAs for spin injection, J. Cryst. Growth **251**, 297 (2003).

[30] A. Gumberidze, M. Trassinelli, N. Adrouche, C. I. Szabo, P. Indelicato, F. Haranger, J. M. Isac, E. Lamour, E. O. Le Bigot, J. Merot, C. Prigent, J. P. Rozet, and D. Vernhet, Electronic temperatures, densities, and plasma X-ray emission of a 14.5 GHz electron-cyclotron resonance ion source, Rev. Sci. Instrum. **81**, 033303 (2010).

[31] M. Nastasi, J. Mayer, and J. K. Hirvonen, *Ion-Solid Interactions: Fundamentals and Applications* (Cambridge University Press, Cambridge, 1996).

[32] K. Nordlund, S. J. Zinkle, A. E. Sand, F. Granberg, R. S. Averback, R. E. Stoller, T. Suzudo, L. Malerba, F. Banhart, W. J. Weber, F. Willaime, S. L. Dudarev, and D. Simeone, Primary radiation damage: A review of current understanding and models, J. Nucl. Mater. **512**, 450 (2018).

[33] K. Nordlund, Historical review of computer simulation of radiation effects in materials, J. Nucl. Mater. **520**, 273 (2019).

[34] M. Bratko, K. Morrison, A. de Campos, S. Gama, L. F. Cohen, and K. G. Sandeman, History dependence of directly observed magnetocaloric effects in (Mn,Fe)As, Appl. Phys. Lett. **100**, 252409 (2012).

[35] G. Bertotti, Physical interpretation of eddy current losses in ferromagnetic materials. I. theoretical considerations, J. Appl. Phys. **57**, 2110 (1985).

[36] G. Bertotti, *Hysteresis in Magnetism: for Physicists, Materials Scientists, and Engineers* (Academic Press, New York, 1998).

[37] F. Vidal, O. Pluchery, N. Witkowski, V. Garcia, M. Marangolo, V. H. Etgens, and Y. Borensztein, $\alpha - \beta$ phase transition in MnAs/GaAs (001) thin films: An optical spectroscopic investigation, Phys. Rev. B **74**, 115330 (2006).

[38] J. F. Ziegler and J. P. Biersack, The stopping and range of ions in matter, in *Treatise on Heavy-Ion Science: Volume 6: Astrophysics, Chemistry, and Condensed Matter*, edited by D. Allan Bromley (Springer, Boston, 1985), pp. 93–129.

[39] J. F. Ziegler, M. D. Ziegler, and J. P. Biersack, SRIM - the stopping and range of ions in matter (2010), Nucl. Instrum. Methods B **268**, 1818 (2010).

[40] R. E. Stoller, M. B. Toloczko, G. S. Was, A. G. Certain, S. Dwaraknath, and F. A. Garner, On the use of srim for computing radiation damage exposure, Nucl. Instrum. Methods B **310**, 75 (2013).

[41] K. Nordlund, J. Keinonen, M. Ghaly, and R. S. Averback, Coherent displacement of atoms during ion irradiation, Nature (London) **398**, 49 (1999).

[42] A. F. Calder, D. J. Bacon, A. V. Barashev, and Y. N. Osetsky, On the origin of large interstitial clusters in displacement cascades, Philos. Mag. **90**, 863 (2010).

[43] S.-P. Kim, H. B. Chew, E. Chason, V. B. Shenoy, and K.-S. Kim, Nanoscale mechanisms of surface stress and morphology evolution in fcc metals under noble-gas ion bombardments, Proc. R. Soc. A **468**, 2550 (2012).

[44] C. Lu, K. Jin, L. K. Béland, F. Zhang, T. Yang, L. Qiao, Y. Zhang, H. Bei, H. M. Christen, R. E. Stoller, and L. Wang, Direct observation of defect range and evolution in ion-irradiated single crystalline Ni and Ni binary alloys, Sci. Rep. **6**, 19994 (2016).

[45] See Supplemental Material at http://link.aps.org/supplemental/10.1103/PhysRevMaterials.8.024406 for additional magnetization curves.

[46] V. Uhlíř, J. A. Arregi, and E. E. Fullerton, Colossal magnetic phase transition asymmetry in mesoscale ferh stripes, Nat. Commun. **7**, 13113 (2016).

[47] L. D. Landau, E. M. Lifšic, E. M. Lifshitz, A. M. Kosevich, and L. P. Pitaevskii, *Theory of Elasticity: Volume 7* (Pergamon Press, Oxford, 1986).

[48] F. R. N. Nabarro, Mathematical theory of stationary dislocations, Adv. Phys. **1**, 269 (1952).

[49] M. Kleman and O. D. Lavrentovich, *Soft Matter Physics: An Introduction* (Springer, New York, 2003).

[50] M. H. Chan, S. K. So, K. T. Chan, and F. G. Kellert, Defect density measurements of low temperature grown molecular beam epitaxial gaas by photothermal deflection spectroscopy, Appl. Phys. Lett. **67**, 834 (1995).

[51] J. F. Gibbons, Ion implantation in semiconductors—Part II: Damage production and annealing, Proc. IEEE **60**, 1062 (1972).

[52] J. W. van der Jagt, V. Jeudy, A. Thiaville, M. Sall, N. Vernier, L. H. Diez, M. Belmeguenai, Y. Roussigné, S. M. Chérif, M. Fattouhi *et al.*, Revealing nanoscale disorder in W/Co-Fe-B/MgO ultrathin films using domain-wall motion, Phys. Rev. Appl. **18**, 054072 (2022).